FIRST THRUST FROM A MICROFABRICATED ATMOSPHERIC ION ENGINE

Daniel Drew, Daniel S. Contreras, and Kristofer S. J. Pister
BSAC, University of California, Berkeley, USA

ABSTRACT

The bulk of current research in the realm of pico air vehicles has focused on biologically inspired propulsion mechanisms. In this work we investigate the use of electrohydrodynamic thrust produced by a microfabricated corona discharge device as a mechanism to create flying microrobots with no moving parts. Electrodes of various geometries are fabricated from a silicon-on-insulator wafer with a two mask process. Electrical characterization is performed to analyze the effect of inter-electrode gap and emitter electrode width on corona discharge and compare findings to simulation. Outlet air velocity and thrust are directly measured to analyze the effects of collector electrode geometry on performance. A roughly 100 cubic millimeter, 2.5mg thruster is assembled with a thrust to weight ratio exceeding 20.

INTRODUCTION

A recent push in the realm of unmanned aerial vehicles has been towards 'pico' air vehicles, defined as having a maximum takeoff mass of 500 mg or less and maximum dimensions of 5 cm or less [1]. Challenges unique to this size scale include decreased lift-to-drag ratio, difficult manufacture and assembly of mechanisms, and the dominance of area-dependent physical phenomenon (e.g. van der Waals force). The most successful work has focused on biologically inspired mechanisms, particularly flying insects, for inspiration. Flapping wing flying microrobots have demonstrated impressive performance [2, 3], but their complexity can make them difficult to design and build and their thrust to weight ratio at a centimeter scale is not much greater than one.

Electrohydrodynamic (EHD) thrust refers to the electrostatically governed motion of charged particles in a neutral medium. Collisions between charged and neutral particles result in a net directional momentum transfer. Since the momentum transfer is more efficient when the charged particles are ions instead of electrons, the neutral gas flow produced via EHD devices is often referred to as an "ion wind." A common method for producing the ions is corona discharge, which has been adopted for commercial applications including electrostatic precipitators and mass spectrometers. The mechanism of corona discharge induced ion wind is illustrated in Figure 1.

Using the corona discharge and associated EHD force for electronic cooling is an active topic of research [4] and commercialization. Propulsion systems based on the ion wind effect were investigated in the early 20th century but saw limited success. More recent EHD propulsion research has focused on devices with sizes on the order of a square meter, with inter-electrode gaps above 10 centimeters [5]. Corona discharge as a mechanism to produce an ion drift current has been separately studied at electrode gaps down to hundreds of micrometers [6].

The theoretical and empirical models of EHD devices that form the foundation of current research were developed by researchers including Christenson, Moller, and Robinson [7,8]. Derivations of EHD thrust, efficiency, and induced air flow velocity are typically simplified with the following assumptions: gas and ion parameters are uniform across the thruster; high ion drift velocity relative to inlet air velocity; and constant ion mobility within the induced space charge [8,9]. This leads to a simple set of equations describing the relationships between applied voltage, V, ion (corona) current, I, induced air flow velocity, u, thrust to power ratio, η, and force, F:

$$F = \beta_1 \frac{Id}{\mu} \tag{1}$$

$$u = g\sqrt{\frac{I}{\rho\mu\beta_2}} \tag{2}$$

$$I = CV(V - V_0) \tag{3}$$

$$\eta = \frac{d}{\mu V} = \frac{1}{\mu E} \tag{4}$$

Where V_0 is the onset voltage of corona breakdown, d is the separation between the electrodes, μ is the ion mobility in air (about 2 cm^2/Vs), ρ is the density of air, and g and C are functions of geometry. β_1 and β_2 are loss coefficients that are functions of electrode geometry.
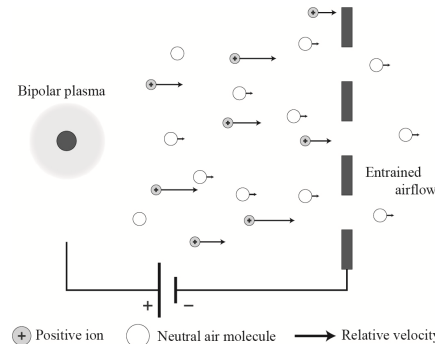

Figure 1: In a positive corona discharge, geometrically asymmetric electrodes result in local field enhancement around the emitter. At some critical field, Townsend ionization results in a sustained bipolar plasma. Positive ions drift in the electric field to the collector. Along the way, they collide with neutral molecules and transfer momentum.

The ion current is space charge limited, with a maximum current density given by Mott-Gurney as $J = \frac{9}{8}\epsilon_0\mu\frac{V^2}{d^3}$. Substituting this into Equation 1 and simplifying, we find the maximum force per unit area that can be achieved from an EHD thruster, which is roughly twice the force density of a traditional parallel plate electrostatic actuator:

$$\frac{F_{max}}{A} = T_{max} = \frac{9}{8}\epsilon_0 E^2 \tag{5}$$

For an EHD thruster with drift field equal to the breakdown field in air of approximately 3MV/m, the maximum thrust is equal to 90N/m^2 at an electrical power to output force transduction efficiency of approximately 2mN/W from (4). At an electric field of 500kV/m, this efficiency rises to 10mN/W at a thrust of 2.5N/m^2, numbers on the same order as flapping wing microrobots [2].

ELECTROSTATIC SIMULATIONS

Finite element analysis was performed with COMSOL Multiphysics in order to investigate the applicability of common corona discharge modeling techniques to devices with the specific size and geometry created in this work.

A positive corona discharge system, where the emission electrode is biased high relative to the collection electrode, can be modelled as having two distinct regions. In the ionization region, Townsend avalanche breakdown due to the high field gradient leads to a sustained plasma. In the drift region, unipolar ions move under the influence of the electric field towards the collector electrode. The thickness of the ionization region, typically on the order of the emission electrode radius, is small enough compared to the inter-electrode gap to allow us to apply some simplifying assumptions [10].

Peek's equations are analytical solutions for the critical breakdown field derived from the Townsend ionization criterion [11]. The equation for the critical field for a parallel wire electrode geometry is shown below:

$$E_{crit} = g_0(1 + \frac{0.301}{\sqrt{r}}) \qquad (6)$$

Where g_0 is the breakdown field strength equal to about 31kV/cm for air and r is the radius of the emission wire in centimeters. Adapted from Peek's analytical solution for the critical potential between parallel wires using the method of image charges, we find the critical potential for corona onset between a wire and a plane:

$$V_{crit} = m_v g_0 r \left(1 + \frac{0.301}{\sqrt{r}}\right) \ln(\frac{2d}{r}) \qquad (7)$$

Where d is the distance between the electrodes and m_v is a coefficient determined by the surface properties of the emitting wire, e.g. m_v=1 for a smooth polished wire.
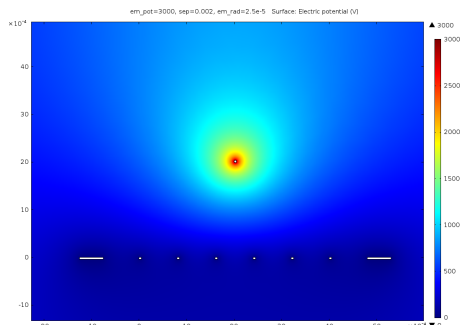

Figure 2: The COMSOL FEA electrostatics module was used to solve for corona discharge inception voltage based on the critical surface field found from (6). The actual grid geometry was used, but the emission wire was modeled as a circle with diameter equal to the wire's width.

EXPERIMENTAL METHODS

Devices are fabricated in a two mask SOI process and individually plasma diced. The corona emitter wires have cross sections ranging from 10μm x 40μm to 50μm x 40μm. The collection grids were typically 6mm squares, with 50μm wires on 500μm centers, a compromise between smooth electric fields (approximating a point-plane system) and lower air flow resistance.

For electrical characterization, glass cover slips are used to vary the inter-electrode distance (Figure 3). High voltage was supplied to the emitter wire by a Gamma High Voltage 10kV supply and current was measured by a benchtop ammeter connected to the collector grid. The power supply is current limited to protect the ammeter. Contact is made with tungsten probe tips.
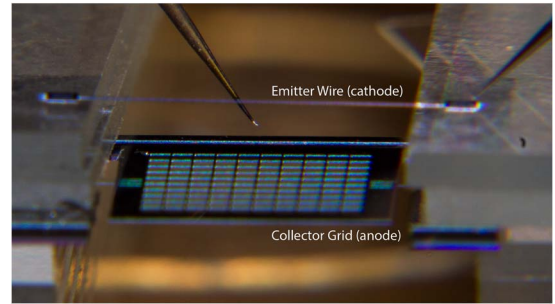

Figure 3: Electrical testing was performed at a probe station. Glass cover slips were used to vary the inter-electrode distance and contact was made via tungsten probe tips. The collector grids were elevated from the probe station chuck by glass slips.

Outlet air velocity measurements were performed using a TSI AVM430 hot wire anemometer placed two millimeters below the collector grid.

RESULTS AND DISCUSSION

The presented data is from a range of fabricated devices, replaced when failure during testing caused obvious damage (e.g. arcing events).

Electrical Characterization

Figure 4 shows measured voltage versus current relationships for devices with three different inter-electrode spacing. A 50μm wide emitter wire is used for each. Figure 5 shows measured IV curves from devices with a constant inter-electrode spacing and varying emitter wire widths.

Plotting I/V as a function of V allows us to relate this gathered electrical data to the Townsend relationship (3). The value of C can be found from the slope, while the intercept represents the corona onset potential. Onset potential found by this method, through the simulation method described previously, and by Peek's analytical formula (7) are shown in Table 1. It is important to note that both the Peek's equation and the simulation method treated the emitting wire as having a circular cross section equal to the wire width instead of the actual rectangular cross section.
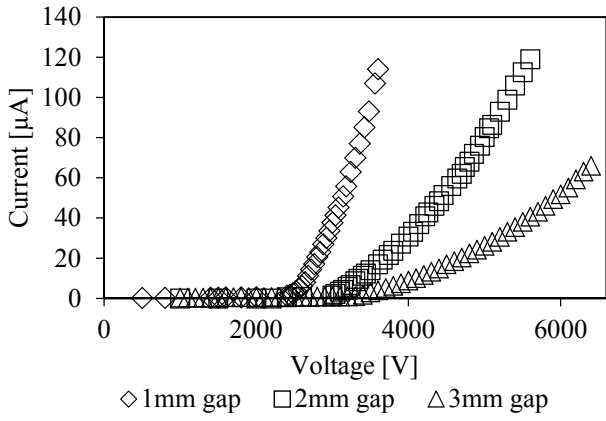
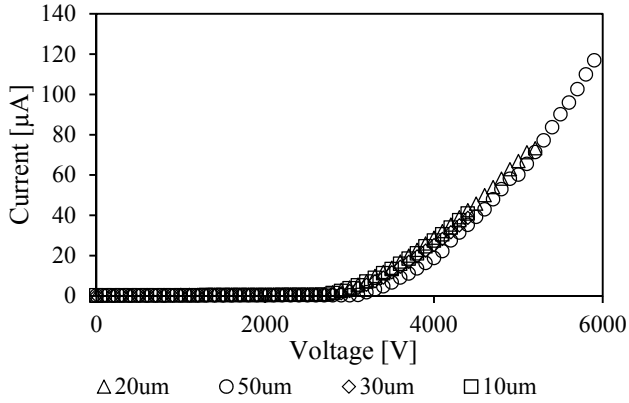*Figure 4: Current versus voltage for varying inter-electrode gaps: 50μm wide wire, 6x6mm grid.*

Figure 5: Current versus voltage for varying emitter wide widths: 2mm inter-electrode gap, 6x6mm grid.

Table 1: Corona inception voltage (in kV) calculated by three different methods for varying electrode geometries.

Width (μm)	10	20	30	50		
Gap (mm)	2	2	2	1	2	3
Peek's	1.45	1.89	2.21	2.31	2.67	2.89
Sim.	1.50	2.00	2.35	2.50	2.85	3.25
Exp.	2.76	2.75	2.85	2.51	2.99	3.28

The results show that scaling the rectangular wire width does not strongly correlate with a decreased corona inception voltage as predicted from our circular cross section approximation. The experimental results for varying gap distance of the 50μm wire agree with simulated and analytical results within 10%, indicating that the grid collector electrode can be modeled as a flat plate as in (6) and (7).

Thrust Measurements

Thrust produced by the engines was first characterized indirectly by the outlet air velocity as measured by hot wire anemometer. The results for 2mm and 3mm electrode gaps with a 50μm wide wire over a 6mm grid are shown in Figure 6.
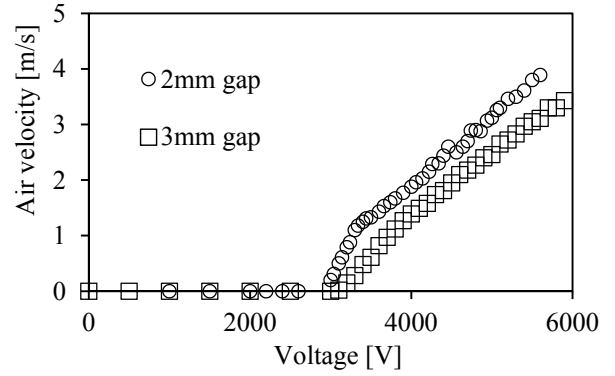

Figure 6: Air velocity versus voltage for varying inter-electrode gaps: 50μm wide wire, 6x6mm grid.

Using the grid without its surrounding frame as the control area, thrust can be deduced from the simple mass flow equation, with A representing the flow outlet area, ρ the density of air, and v_e the outlet flow velocity:

$$F = \dot{m}v_e = \rho A v_e^2 \qquad (8)$$

Thrust was then measured directly by assembling a thruster on the end of a roughly one-meter long balsa wood pendulum with a pin pivot at the top. With the total mass and center of mass known, observing the angular deflection at the tip of the rod and solving the torque balance equation determined the output force. The resulting rod deflection for various data points is shown in Figure 9. Tests were performed with a 50μm wide wire and a 2mm electrode gap.
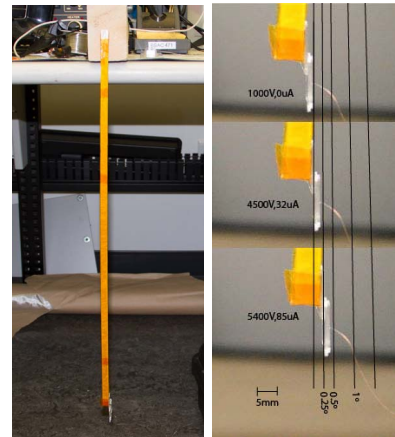

Figure 8: Direct thrust measurement by deflection of a physical pendulum. Current and voltage information was collected alongside video and then still frames were extracted to take individual data points.

The forces, measured directly by the deflection of the pendulum and indirectly by the outlet air velocity, are compared to the theoretical electrostatic force given by (1) to find the geometric loss factor. The two methods agree to within 20% and yield an average loss factor of 48% ($\beta_1 = 0.52$). These results are shown below in Figure 7. Possible sources for this loss factor include drag on the grid wires, horizontal force vector components due to electrode asymmetry, and atmospheric conditions affecting ion mobility.
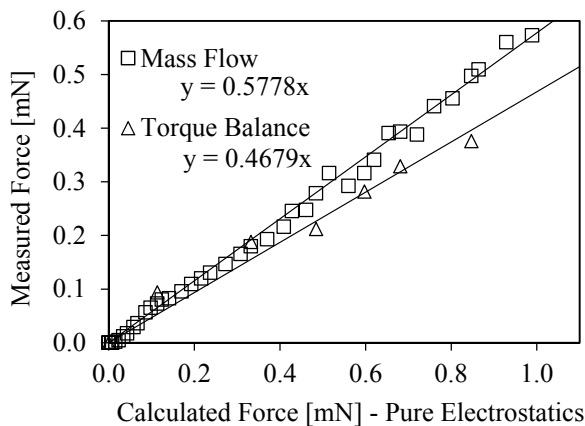
Figure 7: Plotting theoretical electrostatic force from (1) versus experimentally measured force from (8) and (9) for extraction of the geometric loss factor.

Outputs were stable over a roughly ten second period per each data point during the mass flow experiments. Devices could be retested with consistent results after the thirty-minute experiment was complete.

Microassembly

Dielectric standoffs as tall as the desired inter-electrode gap are necessary to produce a low-mass free-standing device with the microfabricated electrodes. Re-designed structures include an attachment mechanism consisting of guiding slots and locking cantilevers. Coated silica capillary tubes with 450μm OD and 25μm wall thickness were inserted into these points and then secured with UV-cured epoxy applied by probe tip. This process leads to the type of device shown in Figure 9, with a total mass of 2.5mg.
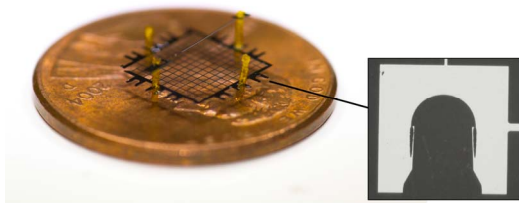

Figure 9: The microfabricated silicon components and silica capillary tubes were assembled by hand. This roughly 100 cubic millimeter device has a mass of about 2.5mg. Inset: Attachment mechanism with guiding slot and locking cantilevers.

CONCLUSIONS

Microfabricated silicon electrodes were used to characterize millimeter-scale corona discharge for a rectangular wire to grid geometry. Output thruster force was measured directly and indirectly to assess the geometric loss factor calculated by divergence from the theoretical electrostatic force. A free-standing wire-grid thruster with silica tube electrode standoffs was assembled: its total mass is about 2.5mg, and the same electrode set has been experimentally measured to produce about 0.5mN of force, a thrust to mass ratio of over 20. Compared to flapping wings, corona discharge based EHD propulsion

requires high voltages and has relatively poor thrust to power ratio. The advantages include being able to use easily fabricated geometries and material, having high force density in N/kg, and DC voltage control of output force. Future work will focus on decreasing the operating voltage, improving assembly techniques, and control schemes for multiple thruster systems. With the kind of thrust to weight ratios achieved in this work it is possible to imagine a future where microrobots fly autonomously, with no moving parts.

REFERENCES

[1] R. Wood, B. Finio, M. Karpelson, K. Ma, N. Perez-Arancibia, P. Sreetharan, H. Tanaka, and J. Whitney, "Progress on 'pico' air vehicles," *The Int. J. Robotics Research*, vol. 31, no. 11, pp. 1292–1302, 2012.

[2] R. Wood, "The First Takeoff of a Biologically Inspired At-Scale Robotic Insect," *IEEE Trans. Robotics*, vol. 24, no. 2, pp. 341–347, 2008.

[3] N. O. Perez-Arancibia, J. P. Whitney, and R. J. Wood, "Lift force control of a flapping-wing microrobot," *Proc. 2011 American Control Conference*, 2011.

[4] A. O. Ong, A. R. Abramson, and N. C. Tien, "Electrohydrodynamic Microfabricated Ionic Wind Pumps for Thermal Management Applications," *J. Heat Transfer*, vol. 136, no. 6, p. 061703, Nov. 2014.

[5] K. Masuyama and S. R. H. Barrett, "On the performance of electrohydrodynamic propulsion," *Proceedings of the Royal Society A: Mathematical, Physical and Engineering Sciences*, vol. 469, no. 2154, pp. 20120623–20120623, Mar. 2013.

[6] R. Tirumala, Y. Li, D. Pohlman, and D. Go, "Corona discharges in sub-millimeter electrode gaps," *Journal of Electrostatics*, vol. 69, no. 1, pp. 36–42, 2011.

[7] E. A. Christenson and P. S. Moller, "Ion-neutral propulsion in atmospheric media.," *AIAA Journal*, vol. 5, no. 10, pp. 1768–1773, 1967.

[8] M. Robinson, "Movement of air in the electric wind of the corona discharge," *Trans. American Institute of Electrical Engineers, Part I: Communication and Electronics*, vol. 80, no. 2, pp. 143–150, 1961.

[9] L. Pekker and M. Young, "Model of Ideal Electrohydrodynamic Thruster," *J. Propulsion and Power*, vol. 27, no. 4, pp. 786–792, 2011.

[10] K. Adamiak and P. Atten, "Simulation of corona discharge in point–plane configuration," *Journal of Electrostatics*, vol. 61, no. 2, pp. 85–98, 2004.

[11] F. W. Peek, *Dielectric phenomena in high voltage engineering*. New York: McGraw-Hill, 1915.

CONTACT

D. Drew; ddrew73@berkeley.edu